City and Environment Interactions 27 (2025) 100214

Contents lists available at ScienceDirect

City and Environment Interactions

journal homepage: www.sciencedirect.com/journal/city-and-environment-interactions

Research Articles

Quantitative assessment of factors that influence heat vulnerability in residential areas using machine learning and unmanned aerial vehicle

Jawoon Gu [a], Dongwoo Kim [b], Chulmin Jun [c], Seungwoo Son [d,*]

[a] Korea Water Resources Corporation, 200, Sintanjin-ro, Daedeok-gu, Daejeon, Republic of Korea
[b] Gyeonggi Research Institute, 1150 Gyeongsu-daero, Jangan-gu, Suwon, Gyeonggi-do 16207, Republic of Korea
[c] Department of Geoinformatics, University of Seoul, 163 Seoulsiripdaero, Dongdaemun-gu, Seoul 02504, Republic of Korea
[d] Korea Environment Institute, Bldg. B, 370 Sicheong-daero, Sejong 30147, Republic of Korea

ARTICLE INFO

Keywords:
Unmanned aerial vehicle
Machine learning
Urban thermal environment
Quantitative assessment
Influencing factors
Exploratory data analysis
Confirmatory data analysis

ABSTRACT

Climate change and urbanization have intensified the urban heat island (UHI) effect, significantly impacting urban living environments. While existing studies have yielded valuable insights into macro-scale thermal environments, this study shifts the focus toward microscale residential contexts, where localized urban form and land use patterns critically shape thermal conditions.

In this study, we analyzed the temporal variations in LST in a residential neighborhood of Okgye-dong, Jung-gu, Daejeon, South Korea. High-resolution thermal imagery captured by unmanned aerial vehicles (UAVs) and interpretable machine learning (ML) techniques were used to model and analyze thermal patterns at the microscale. The study site, adjacent to a river and designated as an Urban Regeneration Area, is particularly vulnerable to summer heat.

Exploratory data analysis (EDA) was conducted to examine statistical characteristics and spatial patterns, followed by confirmatory data analysis (CDA) using nonlinear regression models such as CatBoost, Random Forest, and XGBoost. The results showed that the importance of variables influencing LST varied by time of day. However, meteorological variables such as solar radiation, wind, and humidity were not included due to data limitations.

Among the key findings, alley width, shadow ratio, and distance from the river emerged as dominant variables affecting thermal conditions in residential areas. This study contributes to identifying time-sensitive drivers of urban thermal vulnerability by leveraging UAV-based imagery and ML. Based on these findings, we propose specific policy-oriented strategies for heat mitigation in urban regeneration areas, including improving airflow in narrow alleys by removing obstructions or illegal parking, expanding riverside green spaces to enhance cooling effects, and installing vertical shading elements to reduce localized heat stress and improve thermal comfort.

These results are particularly valuable for urban regeneration projects, where thermal vulnerability is often intensified by high building density and limited green infrastructure. The proposed strategies—such as optimizing alley width, increasing shade coverage, and enhancing riverside green spaces—can be effectively incorporated into localized urban redevelopment plans to improve thermal comfort and resilience.

1. Introduction

Owing to rapid urbanization and ongoing climate change, the urban heat island (UHI) effect has emerged as a major environmental issue. Rapid urbanization replaces natural landscapes with impervious surfaces, altering surface radiation, thermal properties, and humidity in urban areas [1]). The thermal properties of asphalt and concrete can ultimately impact climate change and the natural environment [2]. In addition, previous studies report a significantly higher rate of temperature increase in urban areas compared to non-urban areas, compared to that in non-urban areas; this highlights the need for in-depth research on the thermal environment of urban areas [3–6]. Zhang et al. [7] studied changes in Nanjing's urban thermal environment and predicted that by 2030 and 2040, the city's LST would increase by 8.79 % and 10.92 %, respectively, with LST continuing to rise.

The UHI effect not only compromises the quality of life in urban

* Corresponding author.
E-mail address: swson@kei.re.kr (S. Son).

https://doi.org/10.1016/j.cacint.2025.100214
Received 29 December 2024; Received in revised form 27 May 2025; Accepted 31 May 2025
Available online 1 June 2025

areas but also causes health problems for people dwelling in cities; additionally, it also leads to increased energy consumption, thereby posing major challenges for sustainable development. As globalization continues to impact the ecological environment, the ongoing rise in LST increasingly threatens human living and production conditions [8]. Common measures to improve urban thermal environments include river regulation, creation of open spaces, and landscape planting. These nature-based solutions are known to have a cooling effect and may decrease the temperatures of the areas that surround natural elements [9]. For example, according to Fan et al. [10], the temperatures in the areas located near rivers were 3–5 °C lower than those in adjacent built-up areas. This phenomenon may help mitigate the UHI effect.

Recent studies have also emphasized the critical role of surface materials in shaping microclimatic conditions and thermal comfort. Zhang et al. [7] demonstrated that impervious materials such as asphalt and concrete result in elevated LST and reduced thermal comfort levels, whereas permeable surfaces and vegetation-covered areas contribute to more favorable microclimatic conditions. Their ENVI-met simulations revealed that the Physiological Equivalent Temperature (PET) in vegetated zones was significantly lower than in built-up areas, underscoring the importance of surface composition in urban heat mitigation strategies.

Residential areas are more sensitive to heat stress than other types of land use due to densely populated buildings and low green space ratios, which lead to heat accumulation and poor heat dissipation [11–14]. Notably, if an area has a high ratio of populations vulnerable to heat (e.g., elderly or children), the sensitivity of the area to heat stress is high. Huang et al. [13] reported that elderly residents who engage in outdoor activities in a public housing estate were exposed to a significant level of heat stress. This is because the asphalt and concrete surfaces within the housing estate cause an increase in the ambient temperature near the surfaces. This suggests that housing estates may increase the risk of heat-related illnesses, such as heatstroke. Recent longitudinal studies have further emphasized how long-term land cover changes can exacerbate thermal discomfort in urban residential areas. Long-term reductions in green space are known to significantly deteriorate thermal comfort conditions, especially in high-density residential areas. These results underscore the necessity of incorporating thermal comfort assessments into long-term urban redevelopment and land use planning strategies.

Previous studies have shown that the cooling effect of urban water bodies depends on their physical characteristics such as size, shape, and surrounding airflow [15,16]. In addition, spatial imbalances in production, living, and ecological functions also contribute to disparities in thermal comfort across urban areas.

Several studies have attempted to define threshold values of efficiency (TVoE) for the cooling performance of urban green spaces. For example, Le et al. [17] and Yu et al. [18] reported that 0.5 ha was effective in temperate monsoon and Mediterranean cities, while Yang et al. [19] found that 0.69 ha was more appropriate for high-latitude regions. However, the cooling efficiency of green space is also affected by time of day, seasonality, and spatial form, leading to significant variability across studies [20,21]. These inconsistencies highlight the need for context-sensitive urban design when applying green infrastructure for UHI mitigation.

Most previous studies analyzing urban thermal environments used low-resolution satellite images, such as Landsat and MODIS [22]. Although suitable for large-scale cartographic production, these data sources have limitations in capturing spatial variations at the micro-scale. For example, when evaluating the cooling effect of urban parks or green spaces, results based on coarse-resolution satellite imagery often fail to reflect the thermal conditions actually experienced by urban residents. This discrepancy highlights the necessity of using high-resolution datasets for assessing local heat environments. This study addresses this research gap by employing UAV-based high-resolution thermal imagery and interpretable machine learning to analyze localized thermal patterns that are often undetected in conventional satellite assessments.

Compared to satellite-based approaches such as Landsat and MODIS, UAVs offer significantly higher spatial resolution and greater flexibility in data acquisition. This capability is particularly valuable for detecting micro-scale thermal variations—such as narrow alleys, localized shading, and vegetation patches—that are commonly overlooked in coarse-resolution satellite imagery [23,24]. UAVs can operate at low altitudes and capture thermal imagery at user-defined times, allowing targeted observations under specific solar and meteorological conditions, such as during peak irradiance or shadow formation. These advantages are especially important in older or irregular residential areas, where built environments create highly heterogeneous microclimates. When coupled with interpretable machine learning algorithms such as Random Forest and CatBoost, UAV-derived thermal imagery enables the modeling of nonlinear, context-specific patterns in LST. This integration improves the identification of localized thermal drivers and supports microclimate-sensitive planning strategies based on spatially explicit, empirical evidence [25,26].

Machine learning is excellent for processing large amounts of data and analyzing relationships between various variables. In particular, by analyzing various factors influencing thermal vulnerability (e.g., building density, green area ratio, distance from water bodies, etc.) and building a predictive model, thermal vulnerability can be analyzed more precisely. This helps to efficiently identify key factors related to heat stress in various urban environments [25,26]. For example, Zhang et al. [27] used the random forest (RF) algorithm, a representative machine learning model, to predict the surface urban heat island (SUHI) intensity in a region in China. This approach ensures that the measurement of the thermal environment of an urban region is close to that experienced by the people living in the region; thus, this can support effective management and planning of the urban thermal environment. In addition to urban applications, machine learning has also proven valuable in modeling large-scale ecological responses to LST variation. Zhang et al. [7] showed that seasonal changes in global LST significantly influence gross primary production (GPP), with elevated summer temperatures suppressing photosynthetic activity and winter warming enhancing GPP in high-latitude regions. Their findings underscore the versatility of machine learning in capturing nonlinear, spatiotemporal dynamics between land surface processes and ecosystem responses.

While recent studies have increasingly emphasized the roles of vertical canopy structure, combined evapotranspiration–shading cooling dynamics [16], and socio-ecological vulnerability in heat health risk, few have integrated these perspectives using high-resolution UAV data and interpretable machine learning. Most existing UHI studies rely on satellite imagery or field measurements, often lacking the resolution and flexibility required to uncover microscale dynamics within densely built environments. This study addresses this gap by employing UAV-based thermal imagery and interpretable machine learning to identify time-varying key drivers of thermal vulnerability at the neighborhood level, especially within older residential and urban regeneration areas. By doing so, this research contributes to the growing body of literature on localized and time-sensitive UHI mitigation strategies that incorporate structural, ecological, and social dimensions.

This study offers a novel methodological framework that combines microscale thermal data from UAV imagery with interpretable machine learning to analyze dynamic heat vulnerability in aging residential areas. Unlike many prior studies focused either on large-scale spatial correlations or single-time measurements, this approach captures time-varying patterns of LST across narrow alleys, localized shade, and proximity to water bodies. It also addresses limitations of low-resolution satellite imagery and linear modeling by providing a more granular, flexible, and explanatory assessment of urban thermal environments. The ultimate goal of this study is to analyze the thermal environment of aging residential areas, such as urban regeneration zones, using high-resolution UAV imagery and machine learning techniques. This approach aims to overcome the limitations of conventional satellite-

based analyses and provide insights that can directly support urban planning and thermal risk management.

2. Methods

This study targeted aging residential areas that are vulnerable to heat. Data for the area, acquired using UAVs and thermal imaging cameras, was preprocessed. UAVs and sensors were used to measure thermal environment variables at different time slots. Next, Exploratory data analysis (EDA) was conducted to identify patterns in the acquired data and assess their impact on the urban thermal environment. Furthermore, independent variables potentially influencing the thermal environment in the residential area were examined, with a focus on alleys where residents' activities and movement take place. Confirmatory data analysis (CDA) was conducted to evaluate various machine learning (ML) models and select the most effective one; this analysis also highlighted the importance of independent variables for effective urban thermal environment management. The research flowchart is presented in Fig. 1.

2.1. Selection of study area

The selected study site is a residential area in Gao Bridge, Okgye-dong, Jung-gu, Daejeon, South Korea, located upstream of the Daejeoncheon River (Fig. 2). This area represents the typical topographical features of Daejeon's urbanized basin and has been designated as an Urban Regeneration Area due to its vulnerability to extreme heat. It is characterized by a high proportion of elderly residents and a dense concentration of aging housing. Population density was assessed using a 100 × 100 m grid. The area experiences an average summer temperature of 24.1 °C and a maximum of 39.4 °C, indicating significant risk for heat-related illnesses such as heatstroke.

The study area demonstrates key morphological traits commonly associated with heat-vulnerable urban zones in South Korea, such as narrow alleys, densely packed low-rise housing, limited vegetation, and extensive impervious surfaces. Although not officially designated as an urban regeneration zone, its physical deterioration and microclimatic exposure closely resemble those areas. As such, insights gained from this site may inform urban planning strategies for other neighborhoods with similar environmental and structural vulnerabilities.

2.2. Data collection

Two types of UAVs were used for data collection in this study: the Inspire1 Pro and Mavic Pro (both from DJI Innovations, China). The Inspire1 Pro weighs 2.9 kg and has a maximum flight time of 20 min. The Mavic Pro is lighter, weighing 734 g, with a maximum flight time of 27 min. Both UAVs have a maximum flight speed of 18 m/s. The Inspire1 Pro can fly autonomously and offers stable flight. Additionally, it allows for attachment of a thermal infrared sensor, making it suitable for this study. The Mavic Pro was selected to create a detailed map of alleys in the target area due to its lightweight design and autonomous flight capability exceeding 25 min.

The Zenmuse XT thermal imaging sensor (FLIR Systems, USA) was used for image capture. This sensor provides an image resolution of 640 × 512 pixels, with a spectral band of 7.5–13.5 μm, and operates within a temperature range of −25 °C to 135 °C. The Mavic Pro's optical sensor was a 1/2.3-inch CMOS with an image resolution of 4000 × 3000 pixels. The Inspire1 Pro was equipped with the Zenmuse XT thermal sensor, while thermal images of the study area were captured using the optical sensor on the Mavic Pro. Details of the UAVs and sensors used in this study are provided in Table 1.

UAV flights were conducted at 8:50 AM, 12:20 PM, and 2:50 PM on June 5, 2023, each lasting approximately 30 min. These time slots were selected to represent the typical diurnal progression of LST under clear sky conditions. Specifically, 09:00 represents the morning heating phase, 12:30 captures the midday peak, and 15:00 reflects post-peak thermal retention, enabling comparative analysis of hourly temperature dynamics. This design ensures that temporal variability in the thermal environment is captured without requiring full-day monitoring.

This selection was informed by previous urban climate studies [28,29]and solar irradiance patterns in mid-latitude cities, where LST typically begins to rise rapidly after 08:00, peaks between 12:00 and 14:00, and remains elevated until mid-afternoon before declining. By targeting these time points, the study effectively captures distinct thermal phases—initial accumulation, peak intensity, and delayed retention—without requiring continuous full-day monitoring.

The flight altitude was maintained at approximately 100 m, with a forward and side overlap of 80 % and 60 %, respectively. These parameters were chosen to ensure high spatial resolution and minimize distortion in the resulting imagery. Insufficient overlap or inappropriate altitude can lead to geometric distortions, misalignments, or gaps during orthomosaic generation, directly affecting the accuracy of LST calculations and spatial pattern analyses. Therefore, flight parameters were carefully optimized to enhance the reliability of the UAV-based thermal environment assessment.

The target area for image capture was 250 m × 300 m, with a flight altitude of 120 m and 90 % overlap. Approximately 280 images were collected per flight, and orthoimages were generated using Pix4D Mapper (PIX4D, Switzerland). Eight Ground Control Points (GCPs),

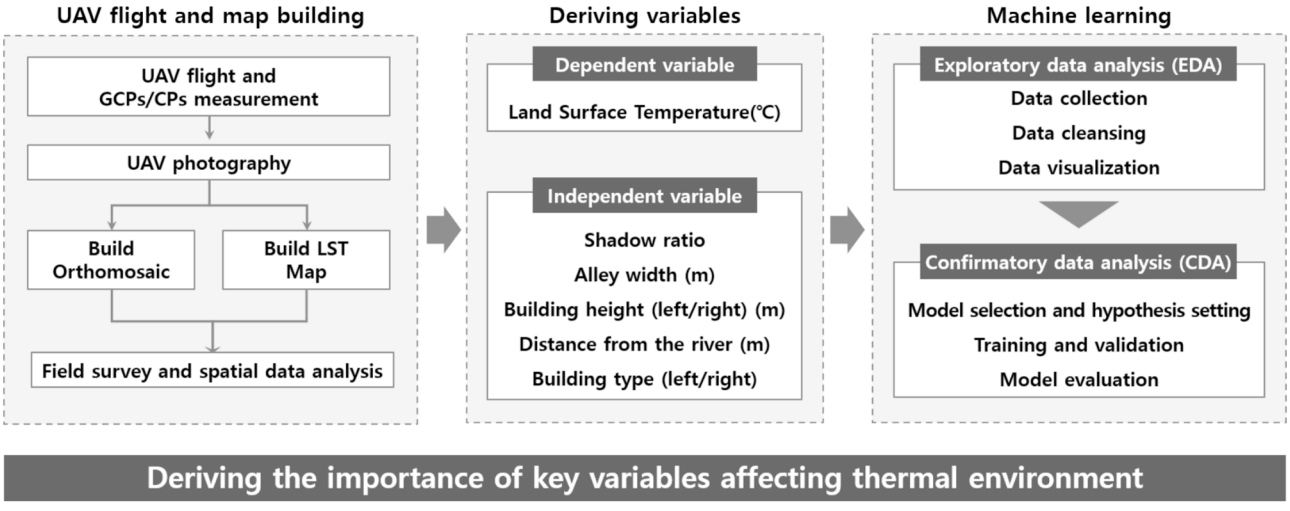

Fig. 1. Research flowchart.

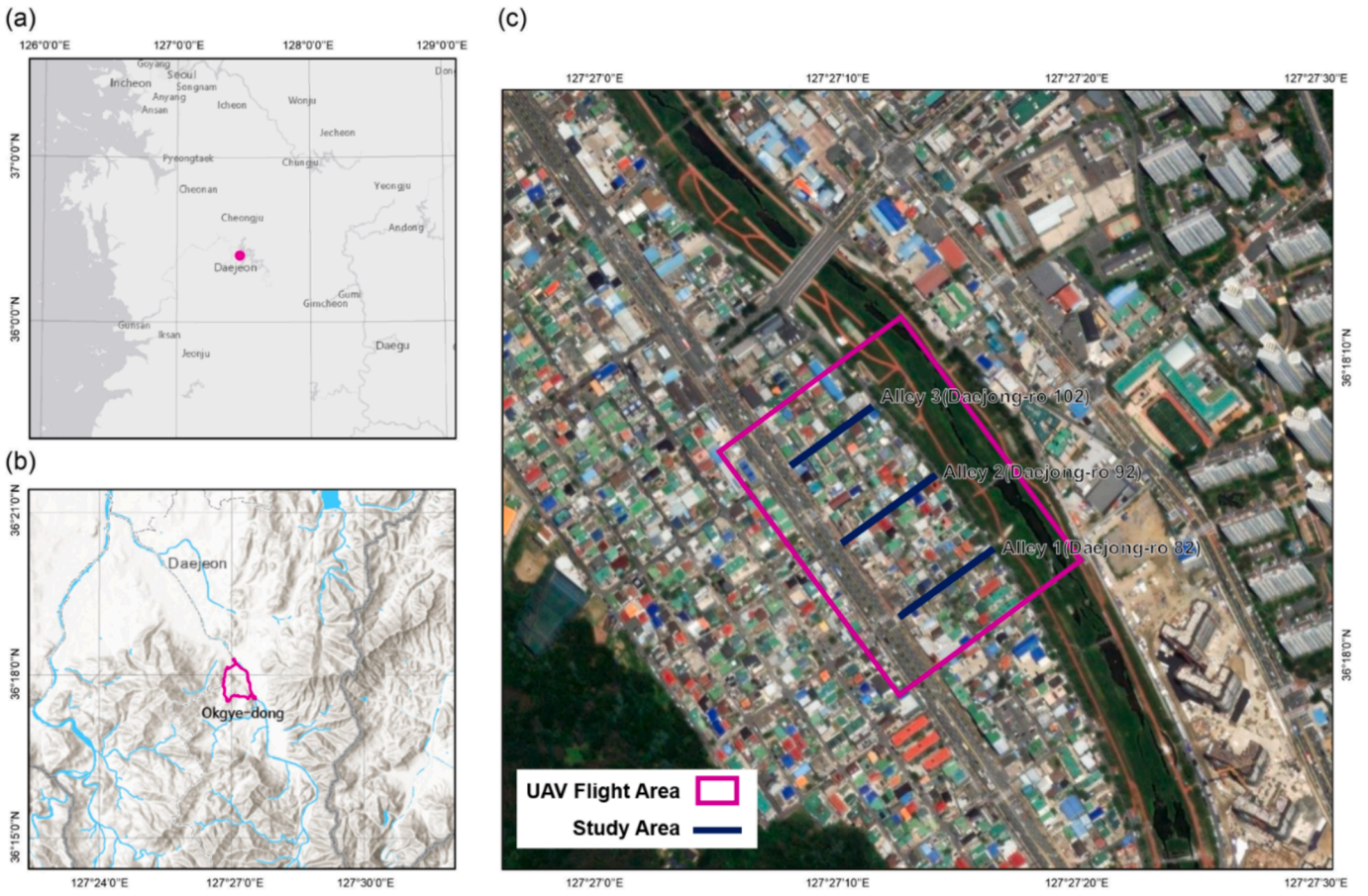

Fig. 2. Maps of the study area. (a) Location of Daejeon in South Korea, (b) Location of Okgye-dong within Daejeon, (c) Map of highlighting the alleys (Alley 1: Daejong-ro 82, Alley 2: Daejong-ro 92, Alley 3: Daejong-ro 102).

Table 1
Specifications of the unmanned aerial vehicles (UAVs) and sensors used in this study.

Type	Specifications	Model	
		Inpire1 Pro with Zenmuse-XT	Mavic Pro with 1/2.3 in CMOS
UAV	Weight (kg)	2.9	0.734
	Maximum flight time (m)	20	27
	Maximum flight speed (m/s)	22	18
Sensor	Image size (pixel)	640 × 512	4000 × 3000
	Spectral Band	Thermal 7.5–13.5 μm	RGB
	Scene range	From −25 °C to 135 °C	–

Abbreviations: complementary metal-oxide semiconductor (CMOS).

measured using Trimble R8s (Trimble Inc., USA), were used to create orthoimages and LST maps.

Temperature and relative humidity were measured in the field using a HOBO U23 data logger (Onset Computer Corporation, USA), with a temperature accuracy of ±0.21 °C. This data logger provided reliable and accurate measurements, complementing the aerial thermal imagery to ensure a comprehensive dataset for thermal environment analysis. Weather measurements, including temperature, humidity, wind direction, and wind speed, were taken at the midpoint of Alley 2 (Daejong-ro 92), located centrally among the three alleys. This location was suitable for collecting representative weather data for the entire study area and served as a basis for thermal environment analysis.

To improve the accuracy of the thermal infrared data, the apparent LST obtained from the Zenmuse XT sensor were calibrated using field-measured air temperature and relative humidity. These values, collected during each UAV flight at a central monitoring point within the study area, were used to correct atmospheric transmission effects through FLIR Tools software. A uniform surface emissivity value of 0.95—commonly used for urban surfaces such as asphalt, concrete, and building walls—was applied across the study site. LST values were cross-validated using a HOBO U23 data logger (Onset Computer Corporation, USA), which has a measurement accuracy of ±0.21 °C. This multi-step correction process ensured the reliability of the UAV-based thermal assessment.

2.3. Exploratory data analysis (EDA)

Exploratory Data Analysis (EDA) was conducted to understand the characteristics of the collected variables and to identify patterns relevant to LST. The key objectives were to calculate basic statistics, identify potential outliers, and visually explore relationships between LST and independent variables. Independent variables included shadow ratio, alley width, building height (left/right), building type (left/right), and distance from the river. For each variable, descriptive statistics such as mean, minimum, maximum, and standard deviation were calculated to assess distributional characteristics. Scatter plots were generated to visually inspect the relationship between LST and each independent variable. Geospatial patterns of LST and independent variables were also visualized using ArcGIS 10.5. In addition, multicollinearity among predictors was examined using the Variance Inflation Factor (VIF), and variables with high collinearity were flagged for further evaluation.

2.4. Confirmatory data analysis (CDA)

Confirmatory Data Analysis (CDA) was conducted to develop predictive models for LST and to identify the key factors influencing thermal patterns in the study area. Eight nonlinear machine learning regression models—including Random Forest (RF), Gradient Boosting, and XGBoost—were used for this purpose. These models were selected for their ability to capture complex and nonlinear interactions among predictors, their robust predictive performance, and their capacity for feature importance analysis. Linear regression and other parametric models were excluded due to their limited ability to represent spatial heterogeneity and nonlinear dynamics in urban thermal environments. Model performance was evaluated using repeated K-fold cross-validation to ensure generalizability and stability across different data splits. Negative mean squared error (MSE) was used as the primary performance metrics. Optimal hyperparameters for each model were determined using grid search, and model residuals were assessed using residual plots to examine fit quality and potential bias. After selecting the best-performing model, feature importance scores were analyzed to quantify the relative influence of each variable on LST predictions. Additionally, one-way ANOVA was performed in the results section to assess statistically significant differences in LST across time periods and alley segments.

3. Result and discussion

3.1. Exploratory data analysis (EDA)

3.1.1. Overview

The study area was divided into three sections: Daejong-ro 82, 92, and 102 alleys (Fig. 3). Each alley represents a distinct subregion within the study area where data were collected and analyzed. The area was divided into these subregions to account for potential differences in thermal environmental characteristics. Descriptive statistics were calculated, and spatial patterns were identified to understand relationships between variables. The data distribution was examined, and outliers were identified. Collected data categories included shadow ratio, alley width, building height (left), building type (left), building height (right), building type (right), distance from the river, and LST measured at each time slot. Descriptive statistics were analyzed to calculate basic metrics for each variable, enabling an understanding of data distribution and identification of factors influencing LST in the region. To analyze the thermal environment, shaded areas were identified for each time slot using orthomosaic images generated from thermal imager captures, and these were verified through field surveys conducted at corresponding times. Alley widths, building heights, and building types were obtained from publicly available data and field surveys. Additionally, distance to the nearest natural green area along the riverside was measured to evaluate cooling effects.

3.1.2. Dependent variables

LST is an important variable for environmental studies; it represents the temperature of the ground surface and is essential data for

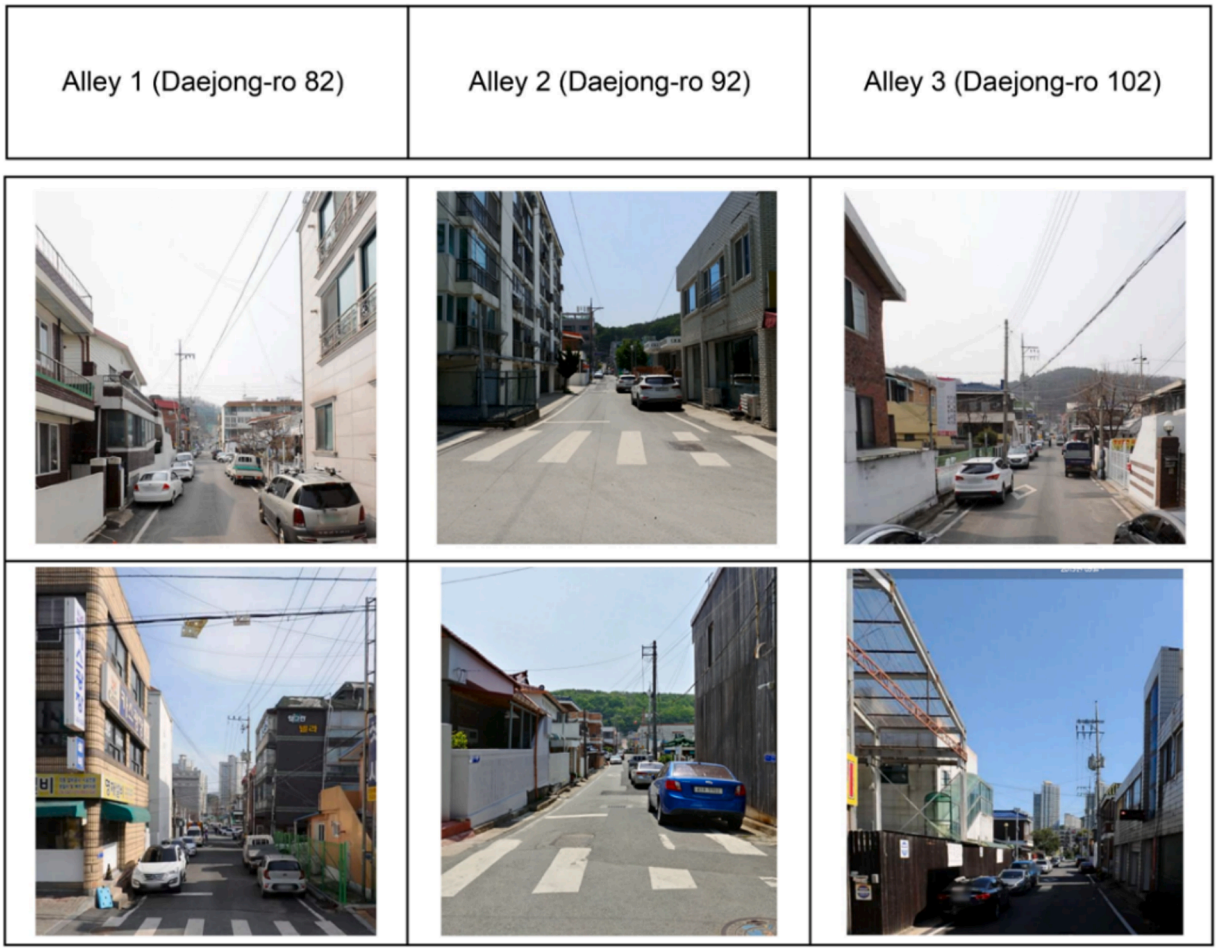

Fig. 3. Photos of the study area. Images of the three alleys considered in this study, captured during the field survey.

environmental monitoring and understanding climate change and the UHI phenomenon. UHI generally means temperature difference, but this study uses LST to analyze the heat distribution in a specific area within the city. LST is closely related to temperature and is an important variable reflecting detailed spatial changes. LST and temperature have a strong relationship in summer, and the two variables show similar patterns in spatial distribution [30]. This shows that LST is a valid indicator that can complement or replace temperature in UHI studies. In addition, LST and temperature show high agreement with each other in UHI evaluation [31]. Cetin et al. [32] emphasized that LST is a variable that can replace temperature and is useful for assessing the heat risk of a city. LST is highly effective for analyzing the urban heat island phenomenon, as it reflects detailed temperature fluctuations and enables more precise heat distribution analysis than temperature. It is also easily collectible through satellite and UAV data. through satellite and UAV data. Above all, it is suitable for spatial and temporal analysis, so it is useful for spatial decision-making.

LST is influenced by various factors. In this study, the changes in LST were analyzed by time-slot (09:00, 12:30, and 15:00 h) for all the three alleys (Daejong-ro 82, Daejong-ro 92, and Daejong-ro 102) (Table 2). Images were captured by cameras mounted on UAVs, and orthomosaic images for all alleys were constructed from these captures. The study area was segmented, and the mean LST value for each segment was calculated (Fig. 4). Segments with parked vehicles at the time of capture were excluded; the study area was divided at 2 m intervals. All alleys in the study area were paved with asphalt, eliminating the need to consider surface characteristic variations.

At 9:00 h, the mean LST was 29.34 °C across all alleys. Notable differences were observed among the three alleys, with Alley 2 exhibiting the highest mean LST at 31.41 °C and the widest temperature range (24.39 °C–36.73 °C). This may be attributed to its surface characteristics that absorb more solar radiation or retain heat more effectively. Alleys 3 and 1 had lower mean LSTs of 30.20 °C and 26.14 °C, respectively.

At 12:30 h, around solar noon, the mean LST increased significantly to 48.77 °C. Alley 2 again recorded the highest mean LST at 51.07 °C, ranging from 45.54 °C to 54.30 °C. Mean LSTs in Alleys 1 and 3 were 47.54 °C and 47.62 °C, respectively, showing relatively uniform values likely due to the high sun angle and consistent solar exposure.

By 15:00 h, the overall mean LST remained nearly unchanged at 48.79 °C. Alley 2 continued to show the highest mean LST at 51.00 °C and the widest temperature range (45.54 °C–54.17 °C). Notably, Alley 1 (47.80 °C) slightly exceeded Alley 3 (47.52 °C) in mean LST, suggesting that solar heat retention may persist into the late afternoon despite the sun's westward shift.

3.1.3. Independent variables

A comprehensive analysis of factors influencing LST showed that shadow ratio, alley width, building height and type, and distance to the river had significant impacts on LST in the region, despite differing mechanisms. For example, areas with high shadow ratios may be shielded from sunlight, resulting in lower LST. Wider alleys may dissipate heat faster than narrower ones. In addition, High-rise buildings or those with reinforced concrete structures tend to absorb and release more heat than other building types, potentially affecting LST in the region. Additionally, the cooling effect from water evaporation is more pronounced in areas near water bodies, contributing to lower LST.

Alley width plays a significant role in heat accumulation and release in urban microenvironments. Street shape influences wind speed and shadow formation, affecting thermal comfort [33]. Data indicates that alley widths ranged from 1.71 to 7.27 m. The mean width was 4.11 m and the standard deviation was 1.25 m, indicating that the width of the alleys varied widely. Notably, wider alleys release heat faster, while narrower alleys increase the likelihood of heat accumulation. As LST is the dependent variable in this study, Alley width was measured for each time slot, accounting for parked vehicles. When there were parked vehicles, only the alley-width that could serve as the passage for pedestrians was considered; thus, the measured alley width varied depending on the time-slot.

The shadow ratio represents the proportion of an area covered by shadow. Shadows can be created by trees or surrounding buildings, and the LST under tree shade was found to be 7.1 °C lower on average than under non-shadowed areas, which was attributed to reduced radiative flux [34]. In this study, the shadow ratio ranged from 0 (no shadow) to 1 (fully shadowed area) (Fig. 5). The mean value of the shadow ratio was 0.34, indicating that the measurements were conducted when about 30 % of the area was in the shadow (on average). Higher shadow ratios corresponded to lower LST. This is because shadows shield the area from sunlight and reduce heat accumulation. The shaded area was measured by constructing orthomosaic images for each time-slot, using the images collected from a UAV mounted with a thermal imager. These shaded area values were verified through field surveys conducted simultaneously.

Distance from the river was crucial for assessing the cooling effect of the water body. The large river has cooling and humidifying effects during the daytime, and the temperature decrease was up to 3.55 °C, and the distance of influence from the river was 1,741 m [35,36]. The thermal comfort effects of rivers have been studied quite extensively from a macroscopic perspective. To be specific, we considered the distance from the area designated as a natural space; the data indicated that the minimum and maximum distances were 2 and 130 m, with the mean distance being 63.78 m and the standard deviation being 36.39 m. The areas located close to the river exhibited a cooling effect; thus, the LSTs in these areas were likely to be lower. This may be because riparian green spaces absorb solar radiation and the evaporation of water bodies causes a cooling effect in the surrounding regions. Distance was measured from the edge of the natural green space to the center of each segment.

Building height is a key variable influencing LST in urban regions due to its direct relation to shadow formation. The building height not only reflects the human living environment but also influences the urban thermal environment [37]. In the study area, the minimum, maximum, and mean building heights (left) were 0, 14.2, and 6.04 m, respectively; the standard deviation was 3.93 m. For the right side, the minimum, maximum, and mean building heights were 0, 11.9, and 4.79 m; the standard deviation was 3.76 m. In general, tall buildings cast larger shadows and lower the ambient temperature or LST of the surrounding area. In addition, the height of the building can influence the direction and speed of wind.

With respect to building type, we noted a similar effect compared to that of building height. dark-colored building materials exhibited higher LST due to their low albedo or emissivity [38]. Regarding building materials, glass was observed to have the lowest LST, followed by bright-

Table 2
Descriptive statistics of LST for each time-slot and alley.

Class	09:00 h				12:30 h				15:00 h			
	Mean	Min	Max	STD	Mean	Min	Max	STD	Mean	Min	Max	STD
Alley 1 (Daejong-ro 82)	26.14	20.12	30.66	2.68	47.54	42.52	49.88	1.87	47.80	43.74	50.73	1.85
Alley 2 (Daejong-ro 92)	31.41	24.39	36.73	2.57	51.07	45.54	54.30	1.60	51.00	45.54	54.17	1.98
Alley 3 (Daejong-ro 102)	30.20	21.80	34.82	2.57	47.62	43.52	50.78	1.96	47.52	42.52	49.88	1.60
ALL	29.34	20.12	36.73	3.43	48.77	42.52	54.30	2.46	48.79	42.52	54.17	2.41

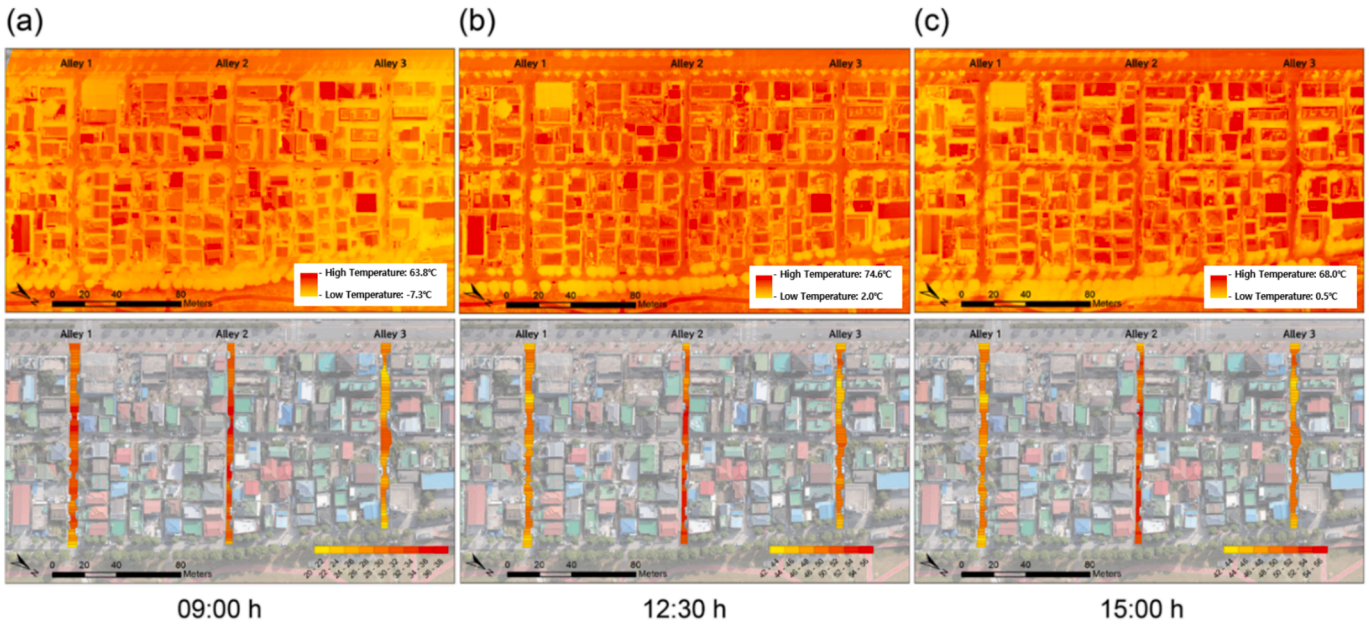

Fig. 4. LST distribution at three time slots. The top row displays thermal infrared images of the study area captured by UAV, while the bottom row shows RGB orthophotos overlaid with average LST values divided by sections in each alley (Alley 1, Alley 2, Alley 3). The color gradient represents the temperature range from low (yellow) to high (red), as indicated in the legend. (a) 09:00 h, (b) 12:30 h, (c) 15:00 h. (For interpretation of the references to color in this figure legend, the reader is referred to the web version of this article.)

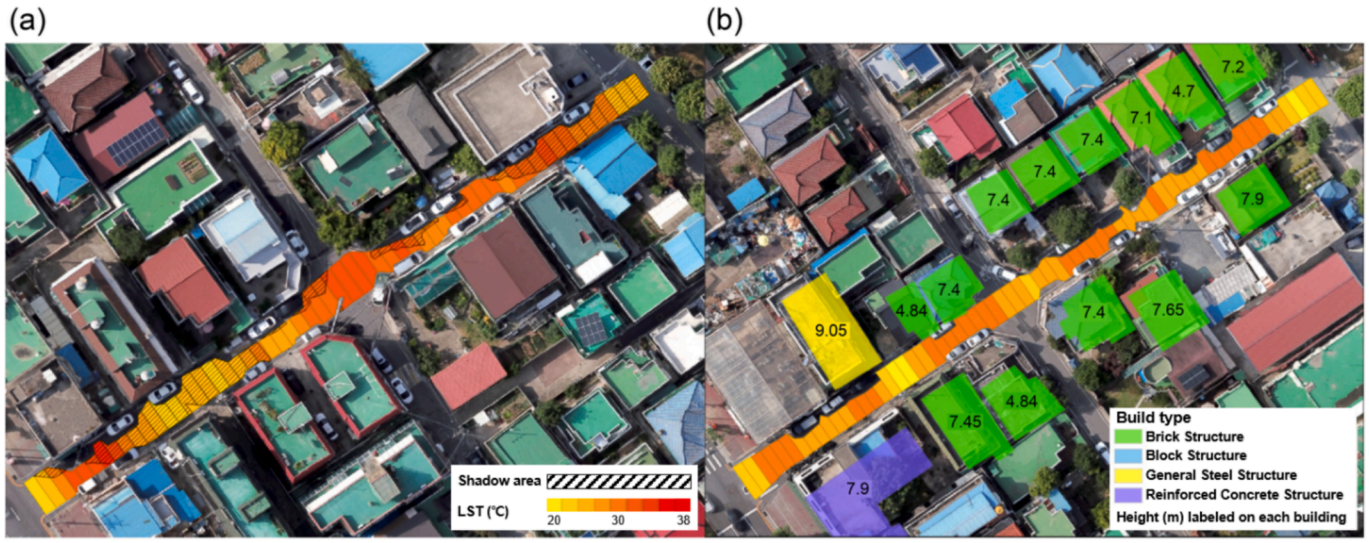

Fig. 5. Shade areas in the study region. Example the areas in shade, with respect to the segment (a) and building type and height (b).

colored building materials. On the other hand, dark-colored building materials, such as steel or black bricks, were observed to have the highest LST [39]. In this study, the building types on the right and left sides were divided; when a building was present, the building types were classified into reinforced concrete, general steel, block, and brick structures. For open spaces without buildings, the space was categorized as impervious or pervious surfaces. The impact on LST varied depending on the building type. For example, an alley adjacent to a green space may have a cooling effect. Publicly available data was used for obtaining the building-related data, and the reliability of the data was verified through field surveys. In segments where buildings were present, the values were set based on the measured height, and in segments with no adjacent buildings, the building height was set to 0. Details are provided in Table 3.

Table 3
Number of buildings by type.

Type		Left side	Right side
Building	Brick structure	92	89
	Block structure	7	13
	General steel structure	8	–
	Reinforced concrete structure	37	24
Open space	Impervious surface	39	58
	Pervious surface	5	4

3.1.4. Statistical overview and bivariate correlation analysis

Descriptive statistics of the independent variables used in this study are summarized in Table 4. Alley width ranged from 1.71 m to 7.27 m,

Table 4
Descriptive statistics of independent variables.

Independent variables	Mean	Standard Deviation	Min	First Quartile	Second Quartile	Third Quartile	Max
Shadow ratio	0.34	0.37	0	0	0.2	0.62	1
Alley width (m)	4.11	1.25	1.71	3.23	3.95	5.18	7.27
Building height (left) (m)	6.04	3.93	0	0	7.4	7.5	14.2
Building height (right) (m)	4.79	3.76	0	0	4.84	7.9	11.9
Distance from the river (m)	63.78	36.39	2	32	64	94.5	130
Building type	–	–	–	–	–	–	–

with a mean of 4.11 m, indicating notable variability across the study area. Shadow ratio values ranged from 0 to 1.0, with an average of 0.34, suggesting that roughly one-third of the surface area was typically shaded during data collection. Building heights and distances from the river also exhibited considerable variation, reflecting diverse microclimatic conditions within the study segments.

To explore the linear relationships between LST and individual independent variables, Pearson correlation coefficients were calculated for each time slot (09:00, 12:30, and 15:00). Fig. 6 presents a heatmap summarizing the strength and direction of these correlations. Among the predictors, alley width exhibited the strongest negative correlation with LST during the morning ($r = -0.51$ at 09:00), suggesting that narrower alleys may contribute to greater heat accumulation in early hours. In contrast, shadow ratio showed its most negative correlation in the afternoon ($r = -0.50$ at 15:00), implying that shading becomes increasingly important as solar radiation intensifies. Distance from the river showed weak and inconsistent correlations, with a weak negative relationship in the morning ($r = -0.16$) and midday ($r = -0.15$), but a slight positive relationship in the afternoon ($r = 0.13$). Building heights exhibited minimal correlation across time slots, indicating that their effect may be more context-dependent or nonlinear.

In addition to correlation analysis, variance inflation factor (VIF) was calculated to assess potential multicollinearity among the continuous independent variables. Across all time slots, VIF values were well below the conventional threshold of 5, with most ranging from 1.1 to 1.7. These results indicate that the variables used in this study are statistically independent and that multicollinearity does not pose a concern in subsequent regression or machine learning models.

Building type variables (BtypeL and BtypeR), being categorical, were excluded from both the correlation and VIF analyses. However, they were incorporated into the machine learning models using appropriate categorical encoding techniques to ensure their influence on LST was adequately considered.

3.2. Confirmatory data analysis (CDA)

3.2.1. Overview of confirmatory data analysis (CDA)

In this study, eight nonlinear regression models were employed to predict land surface temperature (LST) and compare their predictive performance: Decision Tree, Extra Trees, AdaBoost, XGBoost, LightGBM, CatBoost, Random Forest, and Gradient Boosting. The analysis was conducted across three time slots (09:00, 12:30, and 15:00 h) to account for temporal variations in surface heating. Model performance was evaluated using repeated cross-validation, and the primary metric was negative mean squared error (MSE), which provides a reliable indicator of model accuracy by penalizing larger errors more heavily. Optimal hyperparameters for each model were identified using grid search, which exhaustively evaluates combinations of parameters to determine the best configuration. After selecting the best-performing model for each time slot, feature importance analysis was conducted to identify the key predictors influencing LST.

The eight models were selected based on their suitability for handling nonlinear relationships, high-dimensional data, and multicollinearity—common characteristics of environmental datasets (Table 5). Ensemble tree-based models such as RandomForestRegressor, XGBRegressor, LGBMRegressor, and CatBoostRegressor are widely used in environmental modeling due to their strong predictive performance, ability to model complex feature interactions, and interpretability. DecisionTreeRegressor was included as a baseline model for comparison. AdaBoost and GradientBoosting were chosen for their effectiveness on small to medium-sized tabular datasets. Deep learning approaches such as artificial neural networks (ANNs) were excluded due to the relatively small dataset size and the study's emphasis on interpretability and feature attribution in the context of urban planning.

DecisionTreeRegressor is a decision tree-based model that divides data into a tree structure for predictions. Each tree node splits data based on specific criteria, with the final prediction calculated at the terminal node. Decision tree predictions are made by splitting data at each node and returning the average or median at the terminal node. The predic-

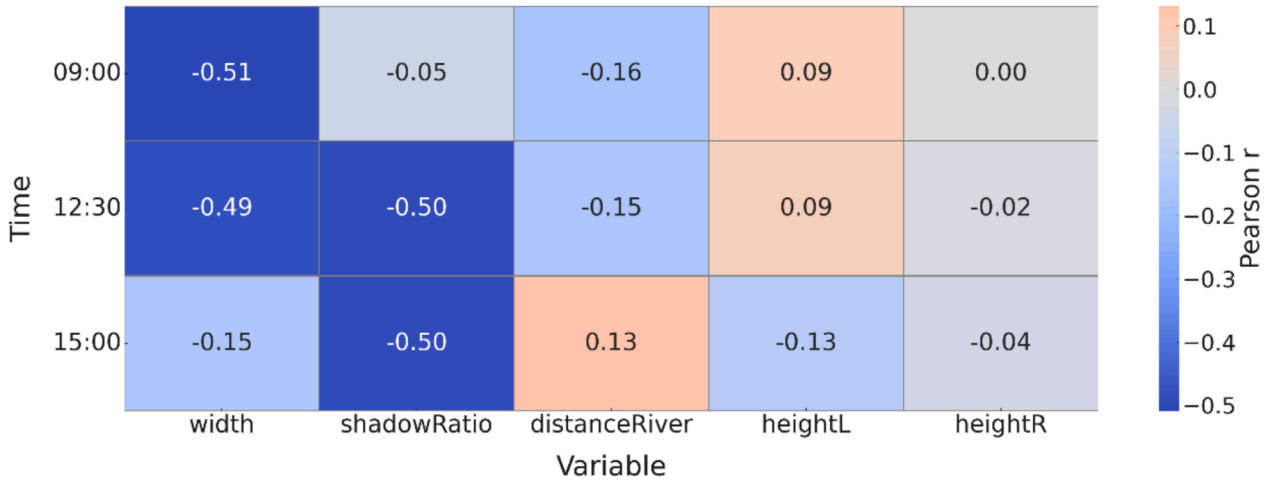

Fig. 6. Pearson correlation between LST and independent variables for each time (09:00, 12:30, 15:00).

Table 5
List of predictive models and hyperparameters used for grid search.

Model	Hyperparameters	Values
DecisionTreeRegressor	max_depth	[3, 5, 10, 15, 20]
ExtraTreesRegressor	n_estimators	[50, 100, 150, 200, 300]
	max_features	['auto', 'sqrt', 'log2']
RandomForestRegressor	n_estimators	[50, 100, 150, 200, 300]
	max_features	['auto', 'sqrt', 'log2']
	max_depth	[3, 5, 10, 15, 20]
AdaBoostRegressor	n_estimators	[50, 100, 150, 200]
	learning_rate	[0.01, 0.05, 0.1, 0.5, 1]
GradientBoostingRegressor	n_estimators	[50, 100, 150, 200, 300]
	learning_rate	[0.01, 0.05, 0.1, 0.15, 0.2]
	max_depth	[3, 5, 10, 15, 20]
XGBRegressor	n_estimators	[50, 100, 150, 200]
	learning_rate	[0.01, 0.05, 0.1, 0.15, 0.2]
LGBMRegressor	n_estimators	[50, 100, 150, 200]
	learning_rate	[0.01, 0.05, 0.1, 0.15, 0.2]
CatBoostRegressor	n_estimators	[50, 100, 150, 200]
	learning_rate	[0.01, 0.05, 0.1, 0.15, 0.2]

tion formula is as follows, and it is the average for the leaf node to which x belongs.

$$f(x) = \frac{1}{n}\sum_{t=1}^{T} y_i$$

This model is easy to handle nonlinear relationships and allows for visual interpretation of data patterns, making it useful for understanding the relationship between LST and physical variables [40].

ExtraTreesRegressor and RandomForestRegressor use ensemble learning to combine multiple decision trees. Each tree is trained using randomly sampled data and variables, which prevents overfitting and improves generalization performance. Predictions of ExtraTrees and RandomForest models are determined by averaging individual tree predictions, as follows:

$$f(x) = \frac{1}{T}\sum_{t=1}^{T} f_t(x)$$

where T is the number of trees and $ft(x)$ is the prediction from each tree. ExtraTreesRegressor adds more randomness so that the trees learn independently, and RandomForestRegressor shows strength in handling complex interactions between various variables [41,42].

AdaBoostRegressor uses a boosting technique that combines multiple weak learners to achieve strong prediction performance. This model improves performance by giving more weight to the prediction errors of each learner. The AdaBoost prediction formula is:

$$f(x) = \sum_{m=1}^{M} a_m h_m(x)$$

Here, $h_m(x)$ is the predicted value of each weak learner, and α_m is the weight of the corresponding learner. This effectively handles the interactions between various variables, which is advantageous in improving prediction performance [43].

GradientBoostingRegressor improves performance through incremental learning, adding new learners to reduce previous errors [44]. The model reduces residuals in the following way:

$$F_{m+1}(x) = F_m(x) + \gamma_m h_{m(x)}$$

Here, $F_m(x)$ is the previous prediction, $h_m(x)$ is the new weak learner, and γ_m is the learning rate.

XGBRegressor and LGBMRegressor are Gradient Boosting extensions optimized for high performance on large datasets through efficient computation. XGBRegressor controls model complexity using the following regularized objective function:

$$F(x) = \sum_{t=1}^{T}\left(\sum_{i=1}^{n} \nabla L(y_i, f(x_i)) + \lambda\|\theta_t\|^2\right.$$

Here, ∇L is the gradient of the loss function, θt is the model parameter, and λ is the regularization term. LGBMRegressor is suitable for large-scale data due to its excellent memory efficiency and learning speed [45,46].

Finally, CatBoostRegressor is a boosting model that automatically processes categorical variables, reducing preprocessing time and improving predictive performance. CatBoost's prediction is expressed as follows:

$$F(x) = F_m(x) + \eta_m \sum_{i=1}^{n} \gamma_i h_i(x)$$

Here, η_m is the learning rate, and $h_i(x)$ represents the contribution of the learner added at each iteration. This model can produce advantageous results, especially in studies that include a lot of categorical data [47].

3.2.2. Model evaluation

The predictive performance of each model was evaluated by splitting the dataset into training and test sets. The training set was used for model fitting, and the test set was used to assess generalization. To ensure reliable performance estimates, we employed the RepeatedKFold cross-validation method, which repeats K-fold cross-validation with multiple random splits. This approach mitigates the influence of any specific data partition, providing a more stable and generalized evaluation.

Prior to model training, one-way analysis of variance (ANOVA) was conducted to statistically assess differences in LST across time slots and alley segments. The results showed significant variation in mean LST among time slots ($F = 2995.27$, $p < 0.0001$), confirming diurnal variation in surface temperature. Significant differences were also observed across alley segments at each time (09:00: $F = 70.52$, $p < 0.0001$; 12:30: $F = 77.15$, $p < 0.0001$; 15:00: $F = 66.90$, $p < 0.0001$), indicating that local spatial characteristics played a key role in shaping thermal patterns. These findings justify modeling each time slot separately and highlight the need to account for both temporal and spatial dynamics in urban heat analysis.

After identifying the optimal model for each time slot, feature importance scores were used to assess the relative influence of each independent variable on LST predictions. Feature importance quantifies each variable's contribution to the model's output, offering insights into the key drivers of urban heat distribution.

Residual analysis was performed to assess the goodness of fit of the models. Residuals, defined as the differences between observed and predicted values, help evaluate how effectively a model captures the underlying data patterns.

Three key diagnostic tests were applied:

- Shapiro–Wilk test was used to assess normality. A low p-value indicated that residuals deviated from a normal distribution, suggesting that model assumptions were not met.
- Levene's test evaluated the homogeneity of variances. A low p-value suggested unequal residual variance, potentially undermining model reliability.

- Durbin–Watson test checked for autocorrelation. A statistic close to 2 indicated minimal autocorrelation, while significant deviations implied temporal dependencies in the residuals.

Several factors may explain discrepancies between model predictions and actual observations:

1. Data limitations: While UAV-based imagery provided high spatial resolution, the study lacked detailed meteorological data (e.g., humidity, wind speed), which are critical to explaining heat distribution. This limited the model's ability to fully capture environmental variation.
2. Model complexity and overfitting: Despite hyperparameter tuning via grid search, some models may have overfit the training data, reducing their generalizability. Differences between cross-validation performance and test results indicate that the models may have been overly tailored to specific training patterns.
3. Spatiotemporal variability: Microscale weather fluctuations—such as cloud cover and wind changes—were not captured in the model. High-resolution data can introduce noise, and the lack of corresponding temporal meteorological data limits predictive accuracy. Incorporating finer-scale environmental inputs is expected to improve future model performance.

3.2.3. Results of model performance evaluation

Table 6 summarizes the performance of all models for each time slot based on negative MSE. Model performance was derived through cross-validation; closer negative MSE values to 0 indicate better performance. For the 9:00 and 15:00 h time slots, the CatBoostRegressor model recorded the lowest MSE, making it the optimal model. At 12:30 h, the RandomForestRegressor model demonstrated optimal performance. The CatBoostRegressor model markedly outperformed other models, especially at 15:00 h, with an MSE of −1.8861.

The superior performance of CatBoostRegressor, particularly in the morning and afternoon time slots, may be attributed to its robustness in handling categorical variables and its use of ordered boosting, which helps prevent overfitting in relatively small datasets. Its ability to capture subtle nonlinear interactions between spatial variables (e.g., shadow ratio, building height) and LST may also contribute to improved prediction accuracy under complex urban conditions. Meanwhile, RandomForestRegressor showed strong performance at midday, possibly due to its ensemble structure and insensitivity to noise, which is beneficial when temporal variability is lower but microclimatic heterogeneity persists.

The optimal hyperparameters for CatBoostRegressor at 9:00 h were learning_rate = 0.05 and n_estimators = 200. The optimal hyperparameters of the CatBoostRegressor model for the time-slot of 15:00 h were: learning_rate = 0.15 and n_estimators = 200. The results indicated significant changes in optimal hyperparameters within the same model, depending on the time slot. The optimal hyperparameters of RandomForestRegressor for the time-slot of 12:30 h were: max_depth = 10, max_features = log2, and n_estimators = 300. ExtraTreesRegressor and LGBMRegressor also demonstrated high and stable performance across time slots. DecisionTreeRegressor, being a relatively simple model, showed lower performance across all time slots. AdaBoostRegressor and GradientBoostingRegressor showed lower performance at certain time slots, despite utilizing boosting techniques.

Table 6
Summary of model performance results by time-slot.

Model	Mean CV Score (neg_MSE)		
	9:00 h	12:30 h	15:00 h
DecisionTreeRegressor	−3.8703	−3.7349	−4.9392
ExtraTreesRegressor	−2.8281	−2.2577	−1.9238
AdaBoostRegressor	−3.3227	−2.7471	−3.7848
XGBRegressor	−3.0845	−2.7294	−2.1099
LGBMRegressor	−2.7612	−2.4676	−2.2792
CatBoostRegressor	**−2.6215**	−2.3940	**−1.8861**
RandomForestRegressor	−2.7632	**−2.2454**	−2.5667
GradientBoostingRegressor	−3.0574	−2.7884	−2.1567

Abbreviations: Coefficient of variance (CV); Negative mean squared error (neg_MSE).

Table 7 shows that the effects of independent variables on LST vary significantly by time slot, primarily due to diurnal shifts in solar radiation, surface heat flux, and urban microclimatic dynamics.

In comparing the three alley segments, Alley 1 consistently exhibited higher LST values across time slots. This can be attributed to its narrow street width, minimal vegetation, and relatively high building density, which restrict airflow and promote heat accumulation. Conversely, Alley 2 displayed relatively lower LST values, likely due to its adjacency to the river, which enhances evaporative cooling, and the presence of more pervious surfaces and shaded areas. Alley 3 showed intermediate characteristics, with moderate shadow coverage but a higher proportion of impervious surfaces, suggesting a transitional thermal behavior between the two extremes.

Alley width was consistently the most influential factor across all time slots, with the highest average importance (22.10 %). Narrower alleys are more enclosed, restricting airflow and increasing multiple reflections of solar radiation between walls. In the morning, when convective mixing is limited and residual heat from previous night's still lingers, heat accumulation in narrow spaces is intensified. At midday, when solar altitude increases, wide alleys receive more direct exposure, while narrow alleys trap both vertical and oblique radiation, sustaining higher LST.

Shadow ratio became most important in the afternoon (15:00 h, 22.06 %) when solar irradiance reaches its peak and direct shortwave radiation dominates. In this time slot, shading plays a critical role in blocking solar gain, especially on hard urban surfaces with low albedo and high thermal mass. The longer shadows cast by buildings during this period can significantly reduce localized LST. In contrast, in the morning and around noon, when diffuse radiation is more prevalent and solar incidence angles are lower, the shading effect is less pronounced, leading to lower importance scores.

Distance from the river maintained relatively high importance throughout the day, especially in the morning (19.63 %) and afternoon (18.07 %). This pattern reflects the cooling function of nearby water bodies via evaporative cooling and convective exchange, which are more effective during times of atmospheric instability or higher humidity contrast. In the early morning, air masses near water retain coolness accumulated overnight, lowering ambient LST. In the afternoon, river-induced breezes and localized moisture can mitigate heat stress in nearby alleys.

Building height (HeightL, HeightR) showed time-varying importance, with stronger effects at 9:00 AM and 3:00 PM. In the morning, taller buildings can block oblique sunlight and reduce direct radiation on surfaces. In the afternoon, tall structures generate long shadows that extend across alleys, increasing shading and altering surface energy balance. Additionally, buildings' thermal mass contributes to delayed heat release, affecting ambient LST differently depending on the time of day.

Building type (BtypeL, BtypeR) had lower importance overall, but showed slight fluctuations depending on time slot. This may reflect differences in thermal inertia, reflectivity, or façade orientation across structural types, affecting how they store and emit heat under changing radiation angles.

In addition to these temporal effects, the spatial variation in LST across alleys also reflects physical differences in the urban form and land cover. Alley segments with higher building density and fewer vegetated areas tended to trap more heat due to limited ventilation, accumulated radiation, and reduced evaporative cooling. The presence of impervious surfaces such as asphalt and concrete also played a role in increasing LST, particularly in locations with low shading and low albedo.

Table 7
Feature importance by time-slot (circled numbers represent the importance ranks).

Feature	Importance			
	09:00 h (CatBoostR.) (unit: %)	12:30 h (RandomForestR.) (unit: %)	15:00 h(CatBoostR.) (unit: %)	Average Importance (unit: %)
Width	① **28.43**	① **27.83**	⑥ 10.04	① **22.10**
shadowRatio	④ 10.97	② **17.26**	① **22.06**	③ **16.76**
distanceRiver	③ **19.63**	③ **16.72**	② **18.07**	② **18.14**
heightR	② **22.68**	④ 14.57	⑤ 12.07	④ 16.44
heightL	⑤ 9.68	⑤ 8.13	③ **18.02**	⑤ 11.94
BtypeL	⑦ 1.23	⑦ 3.31	⑦ 2.97	⑦ 2.50
BtypeR	⑥ 5.13	⑥ 5.55	④ 12.94	⑥ 7.87

Although material-specific emissivity or reflectance values were not directly measured, the building type and surface context provided reasonable proxies for thermal inertia and heat storage. These findings highlight the temporally dynamic nature of urban thermal vulnerability. Effective urban heat mitigation strategies should account not only for static spatial configuration but also for time-sensitive interactions between solar geometry, material properties, and airflow.

This shift in variable importance across time slots can be attributed to daily changes in solar geometry and heat transfer dynamics. In the morning (09:00), lower sun angles limit direct solar penetration into narrow alleys, making factors like alley width more influential due to reduced sky view and restricted ventilation. Narrower alleys tend to trap residual heat from the night and allow less convective dispersion. In contrast, by the afternoon (15:00), solar irradiance is more direct and intense, and the availability of shade becomes a more decisive factor in surface cooling. As a result, shadow ratio becomes increasingly important in mitigating thermal exposure during peak heating hours. These patterns underscore the need for diurnally adaptive strategies in urban heat mitigation.

In addition to individual variable effects, the potential interaction between spatial features may further amplify thermal exposure. For instance, narrow alleys with limited ventilation already retain heat, and when combined with low shadow ratios, the absence of shade leads to intensified solar absorption on impervious surfaces. This combination creates a synergistic effect that can drive LST higher than either condition alone. While this study did not explicitly model interaction effects (e.g., through SHAP interaction values or partial dependence plots), the observed distribution of LST across alleys suggests that these compounded conditions contribute to extreme thermal environments. Future research should aim to quantitatively capture these interaction effects to support more integrated and location-specific mitigation strategies.

3.2.4. Measurements of temperature, relative humidity, and wind direction and speed

At 9:00 h, the temperature was 25.72 °C, with a relative humidity of 63.05 %. By 12:30 h, the temperature had increased to 31.15 °C, while relative humidity had decreased to 42.43 %. At 15:00 h, the temperature and relative humidity further increased to 31.64 °C and 43.86 %, respectively, showing a typical diurnal pattern.

Analysis of wind direction and speed at 09:00 h revealed a dominant southerly wind. The south-southeasterly wind had a high speed of 4–5 m/s, while the southeasterly wind was relatively weak at 1–2 m/s. At 12:30 h, the wind direction shifted to the northwest, with a slight decrease in speed to 2–3 m/s. At 15:00 h, southwesterly winds were dominant, with a speed of 1–2 m/s, only slightly lower than the morning wind speed.

The southerly wind dominance at 09:00 h may be due to local air flows, such as orographic or valley winds, from mountains to the southeast of the study region. The wind direction at 12:30 h may be related to atmospheric convection from daytime ground heating. The wind direction and speed at 15:00 h may result from reduced atmospheric convection activity, causing decreased wind speed. Table 8 presents the detailed information of the measured temperature, relative humidity, and wind direction and speed for each time-slot.

The results indicated that while variables influencing the urban thermal environment varied by time slot, the most important variables on average were alley width, distance from the river, and shadow ratio. river, and shadow ratio. The high importance values of these variables suggest a possible influence of weather conditions. For instance, alley width was important in the morning, while shadow ratio gained importance in the afternoon. These results reflect the impact of solar altitude changes and corresponding shadow patterns; the trends in weather conditions and differences in the impact of variables on LST across time slots were compared with measured data for temperature, relative humidity, and wind direction and speed. However, limitations in measuring wind direction and speed at a microenvironment scale directly impact the thermal environment. Measurement equipment was placed at the study area's center, and measurements were conducted at each time slot, with results plotted into graphs. At 9:00 h, the south and southeasterly winds were strong, indicating a significant impact from the weather. Distance from the river' was important due to the similarity in alley and wind direction and high humidity, which increased its influence on LST. At 12:30 and 15:00 h, the wind direction was northerly and southerly, respectively, intersecting with the direction of the alley; therefore, the variable had relatively little influence on the LST during these time slots. Wind speed at 15:00 h was variable, while at 12:30 h it was relatively gentle, potentially affecting feature importance results. For instance, large portions of the alleys were shaded at 15:00 h, making shadow ratio the most important feature in this time slot. Since alley width correlated with wind direction, its influence was high in certain time slots.

3.2.5. Analysis of residuals

Table 9 presents a summary of the results of the analysis of residuals conducted in this study, with respect to each time slot.

Fig. 7 shows the residual analysis results. The Shapiro–Wilk test was used for testing the normality of residuals. A low p-value indicated that the residuals did not meet the normality condition. Data measured at 09:00 and 12:30 h had very low p-values, indicating non-normal residuals. The data measured at 15:00 h depicted a p-value of 0.5880, indicating that the residuals met the condition of normality.

Levene's test was used to assess variance equality. A low p-value indicated non-homogeneous residual variance. In this study, the p-values for all the measurements for all time slots were low, indicating that the variances of the residuals were not homogeneous. The Durbin-Watson test was used to assess autocorrelation in the residuals. A value closer to 2 suggests a lower probability of autocorrelation in the residuals. For the data measured at 09:00 and 12:30 h, the Durbin-Watson values were 1.1304 and 0.9854, respectively, indicating the possibility of autocorrelation in the residuals. For the data measured at 15:00 h, the Durbin-Watson value was 2.0842, indicating almost zero autocorrelation in the residuals.

Residual analysis showed that at 15:00 h, residuals were normally

Table 8
Depiction of measured temperature, relative humidity, and wind direction and speed by time-slot.

09:00 h	12:30 h	15:00 h
Temperature: 25.72 °C Relative humidity: 63.05 %	Temperature: 31.15 °C Relative humidity: 42.43 %	Temperature: 31.64 °C Relative humidity: 43.86 %
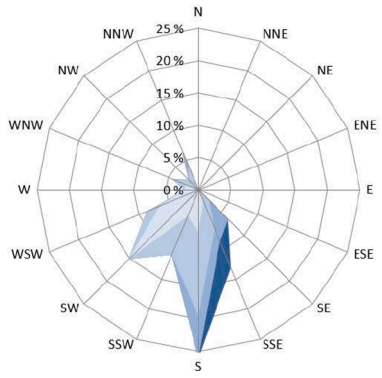	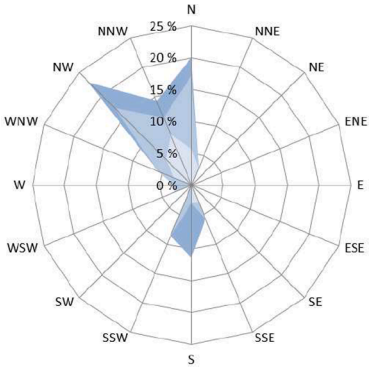	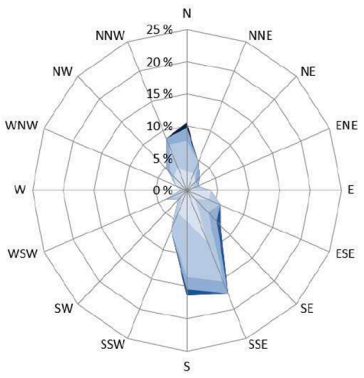

Table 9
Results of the analysis of residuals for each time slot.

Feature	09:00 h (CatBoostR.)	12:30 h (RandomForestR.)	3:00 h (CatBoostR.)
Shapiro–Wilk Test (W)	0.9715	0.9414	0.9936
Shapiro–Wilk Test (p-value)	0.0007	6.2346e−07	0.5880
Levene's Test (p-value)	1.7118e−28	6.9304e−33	1.3018e−43
Durbin-Watson Test	1.1304	0.9854	2.0842

distributed with almost no autocorrelation; however, residual variances were not homogeneous across time slots. This indicated that the model depicted a relatively high predictive performance at a specific time slot; however, the condition of equality of variances was not met. These results indicate that unequal variances may impact the reliability of model predictions.

Moreover, the presence of non-normal and autocorrelated residuals—particularly at 09:00 and 12:30 h—may reduce the reliability of prediction intervals and limit the generalizability of the model to new data. Autocorrelation implies that errors are not independent, suggesting the model may be systematically under- or over-estimating for specific clusters of data. This could result in biased uncertainty estimates or overlooked localized effects. To improve model robustness, future studies could incorporate temporal or spatial features explicitly, or apply models such as GWR or time-aware neural networks that are designed to handle such dependencies.

Notably, residuals at 9:00 and 12:30 h were non-normally distributed with a high likelihood of autocorrelation. This suggests that for these time slots, model predictions may follow a constant pattern, potentially missing specific data patterns. For data measured at 15:00 h, autocorrelation was almost zero, and residuals were normally distributed; however, residual variance remained non-homogeneous. Nevertheless, even at 15:00 h, where residuals were normally distributed, the lack of variance homogeneity suggests that localized anomalies may still be underrepresented. To address this, improving data accuracy through feature engineering is essential. Feature engineering improves predictive performance by transforming existing data or creating new variables. Furthermore, collecting additional data for detailed time-series analysis could improve accuracy with neural network models such as RNN or LSTM.

4. Conclusion

This study analyzed land surface temperature (LST) in three urban alleys located in a residential area of Gao Bridge, Okgye-dong, Jung-gu, Daejeon, South Korea. Measurements were taken at three time slots (09:00, 12:30, and 15:00 h), and nonlinear regression models were used to identify key factors influencing LST. The results revealed that the relative importance of variables varied by time of day. On average, alley width, distance from the river, and shadow ratio were consistently important. Specifically, alley width had greater influence in the morning, while shadow ratio became more dominant in the afternoon. These differences are likely due to diurnal changes in solar altitude and shading patterns.

Residual analysis showed that in some time slots, the residuals did not follow a normal distribution and exhibited autocorrelation, suggesting unresolved temporal dependencies in thermal responses. These findings imply that certain influential variables may have been omitted or insufficiently modeled, and that spatial and temporal autocorrelations were not fully accounted for. Violations of normality and homoscedasticity assumptions could affect the reliability of prediction intervals, while autocorrelation in residuals indicates that localized or sequential thermal patterns were inadequately captured.

One potential cause is the absence of key meteorological or temporal variables, such as solar radiation, wind direction, or lagged temperature values. Incorporating these factors may help capture sequential heat dynamics and reduce residual autocorrelation. Additionally, applying variance-stabilizing transformations (e.g., logarithmic scaling) or adopting models robust to heteroscedasticity (e.g., quantile regression) may improve model reliability. Future studies should explore these enhancements to improve predictive accuracy and better address spatio-temporal dependencies in urban thermal environments.

To enhance the robustness of future predictive models, several improvements can be considered. These include the incorporation of additional meteorological and temporal variables, application of data transformation techniques to normalize residuals, and adoption of spatially explicit modeling approaches such as Geographically Weighted Regression (GWR) or spatio-temporal ensemble methods.

One major limitation of this study is the absence of meteorological variables—such as wind direction, wind speed, and cloud cover—which are essential for capturing transient thermal dynamics but are difficult to collect at microscale resolution. These omitted factors likely reduced the model's ability to explain certain residual patterns. For example, solar radiation and cloud cover directly affect surface heating, while wind

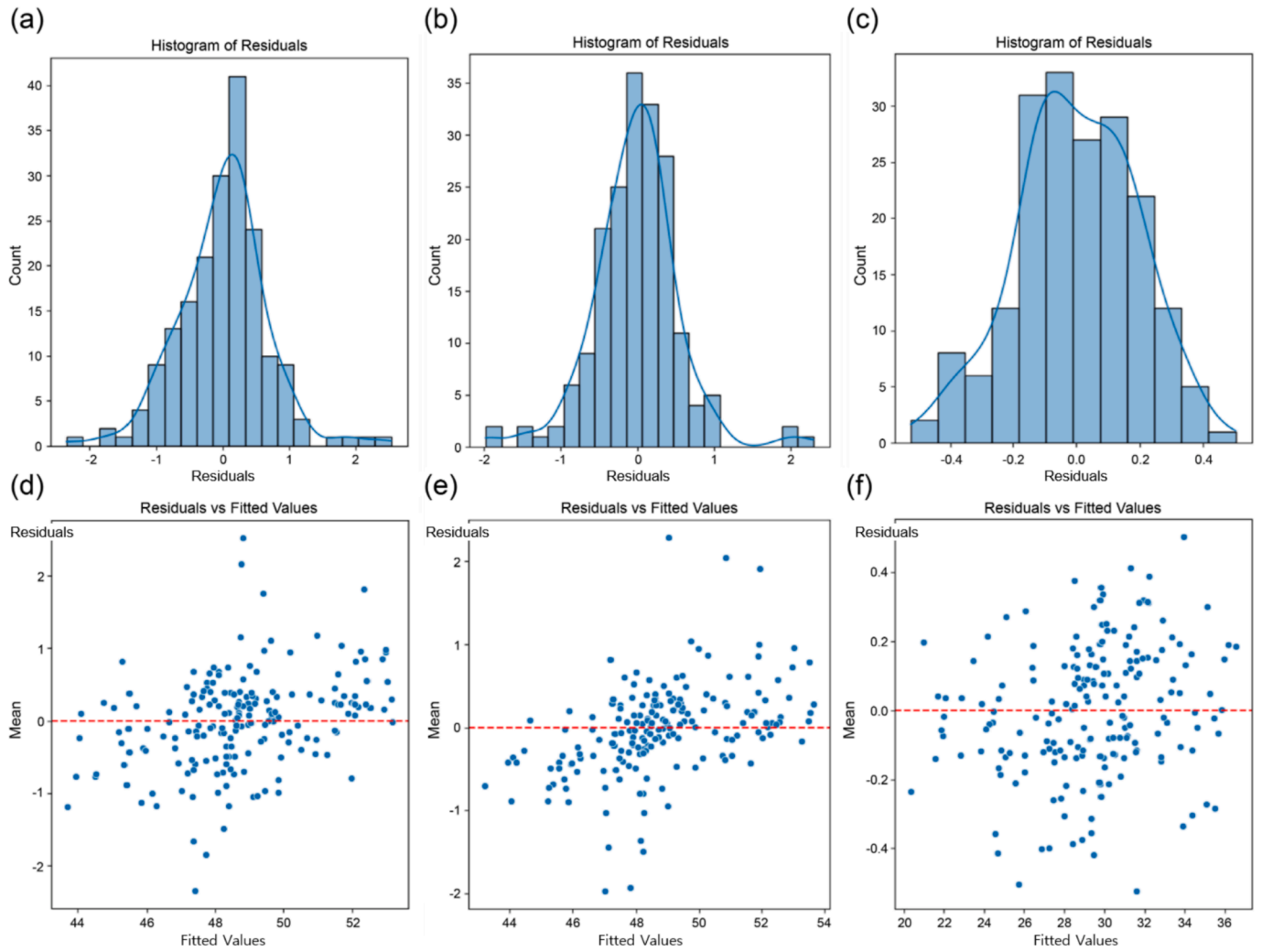

Fig. 7. Results of residual analysis. Histograms of residuals and scatter plots of residuals versus fitted values for each time slot: (a, d) correspond to 09:00 h, (b, e) correspond to 12:30 h, (c, f) correspond to 15:00 h.

dynamics influence convective cooling within narrow urban alleys. Without these variables, the model may have overemphasized spatial predictors and underestimated atmospheric influences. This limitation likely contributed to the presence of non-normal or autocorrelated residuals in specific time slots.

To overcome this, future research should consider deploying compact, localized meteorological sensors (e.g., portable weather stations, IoT-based loggers) across multiple alley segments. These instruments would enable continuous measurement of key parameters such as wind, humidity, and cloud cover, improving both temporal resolution and the calibration of thermal imagery. While GWR was excluded in this study due to the limited spatial scope and concerns about overfitting, it could be reconsidered in larger or more spatially heterogeneous study areas.

Furthermore, although this study identified statistical associations between urban features and LST, it did not fully disentangle the underlying physical mechanisms. For instance, the effect of shadow ratio may vary with building orientation, sun angle, and surface albedo, while river proximity may influence cooling differently depending on airflow and humidity levels. Future research could address this by installing fixed ground-based sensors to collect high-resolution meteorological data or by integrating localized weather forecasts to more precisely capture temporal dynamics.

Based on the results of this study, we recommend that urban planning and design strategies explicitly incorporate the cooling effects of rivers, alley morphology, and shadow-generating features. The machine learning models consistently identified alley width, shadow ratio, and river proximity as the top predictors of LST variation across all time slots. For example, alleys narrower than 3 m were associated with significantly higher surface temperatures, suggesting a need to regulate or retrofit these urban forms to facilitate ventilation and thermal relief.

To support thermal resilience in urban regeneration areas, design guidelines should include:

- Minimum alley width standards to promote airflow
- Installation of vertical shading elements (e.g., trees, awnings, trellises)
- Use of permeable or reflective paving materials
- Preservation and enhancement of riparian corridors for evaporative cooling

In older, high-density neighborhoods with limited capacity for large-scale redevelopment, such interventions can be applied at the micro-scale. Strategies may include removing obstructive street elements (e.g., illegally parked vehicles) to restore ventilation corridors, integrating small green pockets, or selecting reflective facade materials during building renovations. Although GWR was excluded due to spatial constraints in this study, it may prove useful in larger urban domains with spatial heterogeneity.

Despite the utility of the findings, this study did not define precise

threshold values (e.g., optimal alley width or shadow ratio) due to data limitations. Future research should incorporate simulation-based sensitivity analyses or parametric optimization to develop concrete, evidence-based design criteria. Moreover, examining interaction effects between variables—such as between shadow ratio and river proximity—may further enhance the explanatory power of LST models.

The omission of key meteorological variables (e.g., wind direction, humidity, solar radiation, cloud cover) is another limitation. These factors significantly influence microscale thermal dynamics. Future studies should deploy compact urban weather sensors or mobile stations to capture real-time data. Integration of meteorological datasets would also enable better calibration of UAV-based thermal imagery and improve model generalization.

Furthermore, expanding urban green infrastructure represents a promising approach for UHI mitigation. Strategically placed green spaces not only enhance thermal comfort but also improve air quality and urban livability. Prioritizing such interventions in thermally vulnerable neighborhoods would promote environmental equity and resilience.

Methodologically, this study demonstrates the value of combining UAV-based thermal imagery with interpretable machine learning to investigate fine-scale urban heat patterns. Compared to traditional satellite-based analyses, this approach allows for design-level insights tailored to microenvironments. In future work, more advanced or interpretable models—such as convolutional neural networks (CNNs), long short-term memory networks (LSTMs), or explainable AI (XAI) frameworks—could be employed to capture spatiotemporal dynamics more effectively. Combining UAV data with real-time IoT-based environmental sensors will further enhance analytical depth and support practical applications in urban climate adaptation.

Data availability statement

Gu, J. W. (2024). Code for Quantitative Assessment of Factors Influencing Heat Vulnerability in Residential Areas using Machine Learning and UAV Data [Data set]. Zenodo. https://doi.org/10.5281/zenodo.12793156.

CRediT authorship contribution statement

Jawoon Gu: Writing – original draft, Visualization, Software, Resources, Methodology, Data curation. **Dongwoo Kim:** Validation, Investigation, Formal analysis, Conceptualization. **Chulmin Jun:** Formal analysis, Methodology, Validation. **Seungwoo Son:** Writing – review & editing, Supervision, Project administration, Funding acquisition.

Funding

This work was funded by the Korea Environmental Industry & Technology Institute (KEITI) [Grant number: 2021003360001] and the Development of ICT-based Ecosystem Monitoring Technology and AI Algorithms for Flora-Fauna Detection project [Grant number: 2024-010 (R)] funded by the Korea Environment Institute (KEI).

Declaration of competing interest

The authors declare that they have no known competing financial interests or personal relationships that could have appeared to influence the work reported in this paper.

Data availability

I have shared the link to my data/code at the Attach File step.

References

[1] Meng Q, Zhang L, Sun Z, Meng F, Wang L, Sun Y. Characterizing spatial and temporal trends of surface urban heat island effect in an urban main built-up area: a 12-year case study in Beijing, China. Remote Sens Environ 2018;204:826–37. https://doi.org/10.1016/j.rse.2017.09.019.
[2] Lee K, Lim CH. Analysis of the surface urban heat island changes according to urbanization in Sejong City using Landsat Imagery. Kor J Rem Sens 2022;38:225–36. https://doi.org/10.7780/kjrs.2022.38.3.1.
[3] Guo L, Di L, Zhang C, Lin L, Chen F, Molla A. Evaluating contributions of urbanization and global climate change to urban land surface temperature change: a case study in Lagos, Nigeria. Sci Rep 2022;12(1):14168. https://doi.org/10.1038/s41598-022-18193-w.
[4] Habeeb D, Vargo J, Stone B. Rising heat wave trends in large US cities. Nat Haz 2015;76:1651–65. https://doi.org/10.1007/s11069-014-1563-z.
[5] He BJ, Wang J, Zhu J, Qi J. Beating the urban heat: situation, background, impacts and the way forward in China. Ren Sust Energy Rev1 2022;161:112350. https://doi.org/10.1016/j.rser.2022.112350.
[6] Liu Z, Zhan W, Bechtel B, Voogt J, Lai J, Chakraborty T, et al. Surface warming in global cities is substantially more rapid than in rural background areas. Comm Earth Environ 2022;3(1):219. https://doi.org/10.1038/s43247-022-00539-x.
[7] Zhang M, Tan S, Liang J, Zhang C, Chen E. Predicting the impacts of urban development on urban thermal environment using machine learning algorithms in Nanjing, China. J Environ Manage 2024;356. https://doi.org/10.1016/j.jenvman.2024.120560.
[8] Xu C, Huang G, Zhang M. Comparative analysis of the seasonal driving factors of the urban heat environment using machine Learning: evidence from the Wuhan urban agglomeration, China, 2020. Atmosphere (Basel) 2024;15. https://doi.org/10.3390/atmos15060671.
[9] Zhang M, Kafy AA, Xiao P, Han S, Zou S, Saha M, et al. Impact of urban expansion on land surface temperature and carbon emissions using machine learning algorithms in Wuhan, China. Urban Clim 2023;47. https://doi.org/10.1016/j.uclim.2022.101347.
[10] Fan H, Yu Z, Yang G, Liu TY, Liu TY, Hung CH, et al. How to cool hot-humid (Asian) cities with urban trees? An optimal landscape size perspective. Agric For Meteor 2019;265:338–48. https://doi.org/10.1016/j.agrformet.2018.11.027.
[11] Wu Z, Kong F, Wang Y, Sun R, Chen L. The impact of greenspace on thermal comfort in a residential quarter of Beijing, China. Int J Environ Res Public Health 2016;13. https://doi.org/10.3390/ijerph13121217.
[12] Rui L, Buccolieri R, Gao Z, Gatto E, Ding W. Study of the effect of green quantity and structure on thermal comfort and air quality in an urban-like residential district by ENVI-met modelling. Build Simul 2019;12:183–94. https://doi.org/10.1007/s12273-018-0498-9.
[13] Huang J, Chen Y, Jones P, Hao T. Heat stress and outdoor activities in open spaces of public housing estates in Hong Kong: a perspective of the elderly community. Indoor Built Environ 2022;31(6):1447–63. https://doi.org/10.1177/1420326X20950448.
[14] Xiang Y, Chang D, Cheng J. Exploring the correlation between urban microclimate simulation and urban morphology: a case study in Yeongdeungpo-gu, Seoul. In: 2023 IEEE international conference on industrial engineering and engineering management (IEEM). IEEE; 2023. p. 1224–8. https://doi.org/10.48550/arXiv.2310.09779.
[15] Wu Z, Ren Y. A bibliometric review of past trends and future prospects in urban heat island research from 1990 to 2017. Environ Rev 2019;27(2):241–51. https://doi.org/10.1139/er-2018-0029.
[16] Yu Z, Fryd O, Sun R, Jørgensen G, Yang G, Özdil NC, et al. Where and how to cool? An idealized urban thermal security pattern model. Land Ecol 2021;36:2165–74. https://doi.org/10.1007/s10980-020-00982-1.
[17] Le MT, Cao TAT, Tran NAQ. The role of green space in the urbanization of Hanoi city. In: E3S web of conferences. Vol. 97. EDP Sciences; 2019. p. 01013. doi: 10.1051/e3sconf/20199701013.
[18] Yu Z, Xu S, Zhang Y, Jørgensen G, Vejre H. Strong contributions of local background climate to the cooling effect of urban green vegetation. Sci Rep 2018;8(1):6798. https://doi.org/10.1038/s41598-018-25296-w.
[19] Yang G, Yu Z, Jørgensen G, Vejre H. How can urban blue-green space be planned for climate adaption in high-latitude cities? A seasonal perspective. Sus Cities Soc 2020;53:101932. https://doi.org/10.1016/j.scs.2019.101932.
[20] Santamouris M, Ban-Weiss G, Osmond P, Paolini R, Synnefa A, Cartalis C, et al. Progress in urban greenery mitigation science–assessment methodologies advanced technologies and impact on cities. J Civil Eng Manag 2018;24(8):638–71. https://doi.org/10.3846/jcem.2018.6604.
[21] Taha H. Cool cities: Counteracting potential climate change and its health impacts. Curr Clim Change Rep 2015;1(3):163–75. https://doi.org/10.1007/s40641-015-0019-1.
[22] Diem PK, Nguyen CT, Diem NK, Diep NTH, Thao PTB, Hong TG, et al. Remote sensing for urban heat island research: progress, current issues, and perspectives. Rem Sens App: Soc Environ 2024;33:101081. https://doi.org/10.1016/j.rsase.2023.101081.
[23] Rickens B, Tonekaboni NH. Towards high resolution urban heat analysis: incorporating thermal drones to enhance satellite based urban heatmaps. In: ACM web conference 2023 - companion of the world wide web conference, WWW 2023. Association for Computing Machinery, Inc; 2023. p. 707–14. doi: 10.1145/3543873.3587682.
[24] Sidiqui P, Roös PB, Herron M, Jones DS, Duncan E, Jalali A, et al. Urban Heat Island vulnerability mapping using advanced GIS data and tools. J Earth Syst Sci 2022;131. https://doi.org/10.1007/s12040-022-02005-w.

[25] Lyu F, Wang S, Han SY, Catlett C, Wang S. An integrated cyberGIS and machine learning framework for fine-scale prediction of urban heat Island using satellite remote sensing and urban sensor network data. Urban Inf 2022;1. https://doi.org/10.1007/s44212-022-00002-4.
[26] Li F, Yigitcanlar T, Nepal M, Thanh KN, Dur F. A novel urban heat vulnerability analysis: integrating machine learning and remote sensing for enhanced insights. Remote Sens (Basel) 2024;16. https://doi.org/10.3390/rs16163032.
[27] Zhang Y, Liu J, Wen Z. Predicting surface urban heat island in Meihekou city, China: a combination method of Monte Carlo and random forest. Chin Geograph Sci 2021;31:659–70. https://doi.org/10.1007/s11769-021-1215-7.
[28] Loveday J, Loveday G, Byrne JJ, Ong BL, Morrison GM. Seasonal and diurnal surface temperatures of urban landscape elements. Sustainability 2019;11(19):5280.
[29] Kim YJ, Jee JB, Kim GT, Nam HG, Lee JS, Kim BJ. Diurnal variations of surface and air temperatures on the urban streets in Seoul, Korea: an observational analysis during bbmex campaign. Atmos 2020;11(1):60.
[30] Berg E, Kucharik C. The dynamic relationship between air and land surface temperature within the Madison, Wisconsin Urban Heat Island. Remote Sens (Basel) 2022;14. https://doi.org/10.3390/rs14010165.
[31] Sun T, Sun R, Chen L. The trend inconsistency between land surface temperature and near surface air temperature in assessing urban heat island effects. Remote Sens (Basel) 2020. https://doi.org/10.3390/RS12081271.
[32] Cetin M, Ozenen Kavlak M, Senyel Kurkcuoglu MA, Bilge Ozturk G, Cabuk SN, Cabuk A. Determination of land surface temperature and urban heat island effects with remote sensing capabilities: the case of Kayseri, Türkiye. Nat Hazards 2024;120:5509–36. https://doi.org/10.1007/s11069-024-06431-5.
[33] Cárdenas-Jirón LA, Graw K, Gangwisch M, Matzarakis A. Influence of street configuration on human thermal comfort and benefits for climate-sensitive urban planning in Santiago de Chile. Urban Clim 2023;47. https://doi.org/10.1016/j.uclim.2022.101361.
[34] Zaki SA, Toh HJ, Yakub F, Saudi ASM, Ardila-Rey JA, Muhammad-Sukki F. Effects of roadside trees and road orientation on thermal environment in a tropical city. Sustainability (Switzerland) 2020;12. https://doi.org/10.3390/su12031053.
[35] Wang Y, Ouyang W, Zhan Q, Zhang L. The cooling effect of an urban river and its interaction with the littoral built environment in mitigating heat stress: a mobile measurement study. Sustainability (Switzerland) 2022;14. https://doi.org/10.3390/su141811700.
[36] Wang Z, Zhou J, Liu S, Li M, Zhang X, Huang Z, et al. A land surface temperature retrieval method for UAV broadband thermal imager data. IEEE Geosci Rem Sens Lett 2022;19:1–5. https://doi.org/10.1109/lgrs.2021.3100586.
[37] Chen X, Wang Z, Yang H, Ford AC, Dawson RJ. Impacts of urban densification and vertical growth on urban heat environment: a case study in the 4th Ring Road Area, Zhengzhou, China. J Clean Prod 2023;410. https://doi.org/10.1016/j.jclepro.2023.137247.
[38] Prado RTA, Ferreira FL. Measurement of albedo and analysis of its influence the surface temperature of building roof materials. Energy Build 2005;37:295–300. https://doi.org/10.1016/j.enbuild.2004.03.009.
[39] Lee S, Moon H, Choi Y, Yoon DK. Analyzing thermal characteristics of urban streets using a thermal imaging camera: a case study on commercial streets in Seoul, Korea. Sustainability (Switzerland) 2018;10. https://doi.org/10.3390/su10020519.
[40] Loh WY. Classification and regression trees. Wiley Interdiscip Rev Data Min Knowl Discov 2011;1:14–23. https://doi.org/10.1002/widm.8.
[41] Breiman L. Random forests. Mach Learn 2001;45:5–32. https://doi.org/10.1023/A:1010933404324.
[42] Geurts P, Ernst D, Wehenkel L. Extremely randomized trees. Mach Learn 2006;63:3–42. https://doi.org/10.1007/s10994-006-6226-1.
[43] Freund Y, Schapire RE. A decision-theoretic generalization of on-line learning and an application to boosting. J Comput Syst Sci 1997;55:119–39. https://doi.org/10.1006/jcss.1997.1504.
[44] Zemel R, Pitassi T. A gradient-based boosting algorithm for regression problems. Adv Neural Inf Process Syst 2000;13.
[45] Chen T, Guestrin C. XGBoost: a scalable tree boosting system. In: Proceedings of the ACM SIGKDD international conference on knowledge discovery and data mining. Association for Computing Machinery; 2016. p. 785–94. https://doi.org/10.1145/2939672.2939785.
[46] Ke G, Meng Q, Finley T, Wang T, Chen W, Ma W, et al. Lightgbm: a highly efficient gradient boosting decision tree. Adv Neural Inf Process Syst 2017;30.
[47] Prokhorenkova L, Gusev G, Vorobev A, Dorogush AV, Gulin A. CatBoost: unbiased boosting with categorical features. Adv Neural Inf Process Syst 2018;31.

Glossary

ANN: Artificial neural network
CMOS: Complementary metal-oxide semiconductor
CDA: Confirmatory data analysis
CNN: Convolutional neural network
XAI: Explainable AI
EDA: Exploratory data analysis
GIS: Geographic information system
LST: Land surface temperature
LSTM: Long short-term memory
ML: Machine-learning
MODIS: Moderate resolution imaging spectroradiometer
MAUP: Modifiable areal unit problem
negative MSE: Negative mean squared error
RF: Random forest
RNN: Recurrent neural network
SUHI: Surface urban heat island
TVoE: Threshold value of efficiency
UAV: Unmanned aerial vehicle
UHI: Urban heat island